The Astrophysical Journal Letters, 970:L16 (7pp), 2024 July 20 https://doi.org/10.3847/2041-8213/ad5e7e

Understanding the Variability of Helium Abundance in the Solar Corona Using Three-fluid Modeling and Ultraviolet Observations

Leon Ofman[1,2,3], Yogesh[1,2], and Silvio Giordano[4]
[1] NASA Goddard Space Flight Center, Greenbelt, MD 20771, USA
[2] The Catholic University of America, Washington, DC 20064, USA
[3] Visiting, Tel Aviv University, Tel Aviv, Israel
[4] INAF—Astrophysical Observatory of Torino, Via Osservatorio 20, 10025 Pino Torinese, Italy
Received 2024 March 20; revised 2024 June 19; accepted 2024 June 20; published 2024 July 19

Abstract

The variability of helium abundance in the solar corona and the solar wind is an important signature of solar activity, solar cycle, and solar wind sources, as well as coronal heating processes. Motivated by recently reported remote-sensing UV imaging observations by Helium Resonance Scattering in the Corona and Heliosphere payload sounding rocket of helium abundance in the inner corona on 2009 September 14 near solar minimum, we present the results of the first three-dimensional three-fluid (electrons, protons, and alpha particles) model of tilted coronal streamer belt and slow solar wind that illustrates the various processes leading to helium abundance differentiation and variability. We find good qualitative agreement between the three-fluid model and the coronal helium abundance variability deduced from UV observations of streamers, providing insight on the effects of the physical processes, such as heating, gravitational settling, and interspecies Coulomb friction in the outflowing solar wind that produce the observed features. The study impacts our understanding of the origins of the slow solar wind.

Unified Astronomy Thesaurus concepts: Slow solar wind (1873); Solar coronal streamers (1486); Solar ultraviolet emission (1533); Magnetohydrodynamics (1964)

1. Introduction

The solar wind consists typically of approximately 95% protons (H^+), making them the principal constituent by mass, and around 5% helium (predominantly He^{++} or α particles) as the second major constituent, and the corresponding number of electrons stemming from charge neutrality. Here, the abundance of helium in the solar wind is defined relative to protons as $A_{\rm He} = (n_{\rm He}/n_p) \times 100$, where $n_{\rm He}$ and n_p are the concentrations of helium and protons in the solar wind. Understanding variations in helium abundance in the solar wind and solar corona can provide important clues to coronal processes, such as the coronal sources of the slow and fast solar wind, as well as heating and acceleration processes of the solar wind (Neugebauer et al. 1996; Kasper et al. 2007, 2012; Abbo et al. 2016).

The $A_{\rm He}$ was determined with remote-sensing of UV emission in the inner solar corona by using Sounding-rocket Coronagraph Experiment (SCORE), the Helium Coronagraph (HECOR), and HERSCHEL Extreme Ultraviolet Imaging Telescope (HEIT) in the Helium Resonance Scattering in the Corona and Heliosphere (HERSCHEL) payload sounding rocket, launched from White Sands, NM, on 2009 September 14 (Moses et al. 2020). In the photosphere, $A_{\rm He}$ is nearly 8.5% (Grevesse & Sauval 1998; Asplund et al. 2009). However, it remains about 4%–5% in the solar corona due to the First Ionization Potential effects (Laming & Feldman 2001, 2003). The $A_{\rm He}$ can range from 0.1% to more than 10% in the solar wind depending on sources, coronal, and interplanetary modulations and due to the heavy mass of He can account for a significant fraction of the solar wind mass and energy fluxes (Kasper et al. 2007; Alterman & Kasper 2019; Yogesh et al. 2021, 2022, 2023). At times, helium can account for the bulk of the solar wind mass flux at the high-end limit of $A_{\rm He}$. The long-term variability of $A_{\rm He}$ follows the solar cycle (SC) and varies with solar wind velocity (Kasper et al. 2007; Alterman & Kasper 2019; Yogesh et al. 2021). The $A_{\rm He}$ can increase up to 30% in coronal mass ejections (Borrini et al. 1982; Yogesh et al. 2022, and references therein). Although the above results are mainly observed in the solar wind at 1 au, the variation in helium abundance in the inner solar corona was studied using remote-sensing observations (Moses et al. 2020). Previous 2.5D three-fluid models of the slow solar wind that include electrons, protons, and helium as separate interacting fluids demonstrate the variability of A(He) associated with streamer structures, heating, and coronal sources of the solar wind (Ofman 2004a, 2004b; Li et al. 2006; Giordano et al. 2007; Ofman & Kramar 2010). These modeling studies predicted the expected signatures of helium long before the feasibility of such UV observations (see, e.g., Figure 4 in Giordano et al. 2007). Despite these studies, the basic processes that result in the nonuniformity in $A_{\rm He}$ in the solar corona are not well understood in detail so far, due to the complexity of the slow solar wind formation processes (e.g., Abbo et al. 2016). Here, we use an idealized 3D multifluid model to demonstrate the roles of the main ion differentiation physical processes that affect the coronal helium abundance variation in a coronal streamer belt. This is an important problem, as understanding coronal helium abundances variability provides key insights into the formation and coronal sources of the slow solar wind. In Section 2 we present the observational motivation, in Section 3 we present the 3D multifluid model, and Section 4 is devoted to numerical results, with the discussion and conclusions in Section 5.

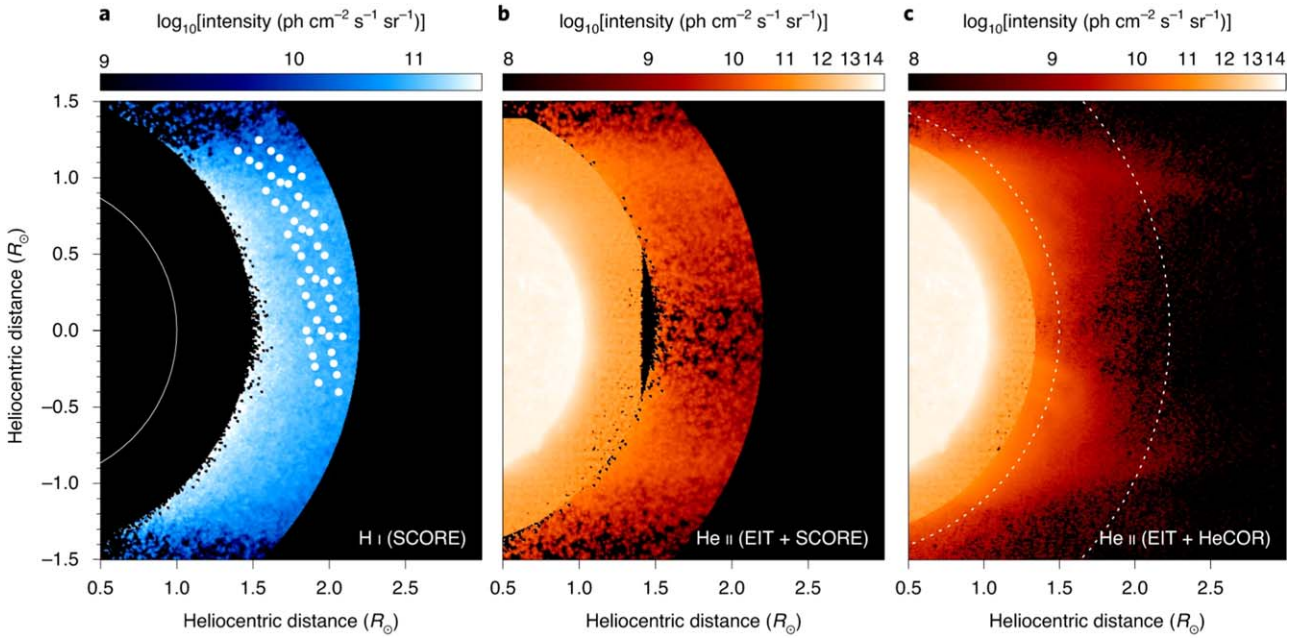

Figure 1. Results from the HERSCHEL experiment on 2009 September 14. Photometric images were acquired in (a) the SCORE H I Lyα and (b) SCORE He II channels spanning the range from 1.5 R_s to 2.2 R_s. The white dots in panel (a) denote the positions corresponding to the coordinated Solar and Heliospheric Observatory Ultraviolet Coronagraph Spectrometer observations. (c) A photometric image was captured in the HECOR He II channel, covering the range from 1.28 to 3 R_s. The EIT image of the stray light-corrected photometric data of He II channel is shown in (b) and (c). Reproduced with permission from Moses et al. (2020).

2. Remote-sensing Observations of Coronal Helium Abundance

Recently, Moses et al. (2020) reported the global helium abundance variability in the solar corona, analyzing the HERSCHEL sounding rocket observations launched on 2009 September 14, at the extended solar activity minimum of cycle 23. The HERSCHEL payload was composed of the SCORE, the HECOR, and the HERSCHEL Extreme Ultraviolet Imaging Telescope (HEIT). SCORE coronagraph is designed to observe the H I (121.6 nm), He II (30.4 nm), and white light, simultaneously from 1.5 R_s to 2.2 R_s (where R_s is the solar radius). HECOR coronagraph was designed to observe the He II (30.4 nm) image from 1.3 R_s to 3 R_s. The disk images of He II were observed by HEIT. The observations from HERSCHEL were complemented by Solar and Heliospheric Observatory Extreme Ultraviolet Imaging Telescope (EIT), the Large Angle and Spectrometric Coronagraph, and the Ultraviolet Coronagraph Spectrometer instruments. In particular, the SCORE was used to obtain the H I and He II emission images of the west limb of the solar corona. Moses et al. (2020) found that the morphology of the H I corona is markedly different from that of the He II corona, owing to significant spatial variations in helium abundance. Figure 1 shows the observations of the H I and He II as reported in Moses et al. (2020). Figures 1(a) and (b) show the images of the H I and He II emission respectively, observed by SCORE. Figure 1(b) shows the EIT image of the stray light-corrected photometric He II channel superposed inside the inner radius of the SCORE field of view. Figure 1(c) shows the He II emission image from HECOR superposed with the EIT image inside the HECOR field of view. Since these observations were focused on the equatorial region in the range of distances from 1.3 to 4 R_s, the contribution of other ions such as Si XI emission to the streamer structure observed in He II is negligible (Fineschi et al. 2003).

It can be seen from Figure 1 that the H I emission is nearly uniformly distributed in nearby equatorial regions, whereas the He II emission is dimmed near the equator as compared to higher and lower latitudes. It was found that the corresponding helium abundance was low ($\leqslant$3%) within $\pm$15° across the equator, and the minimum observed $A_{\rm He}$ was 0.6% near the equator. By using potential ("vacuum") magnetic field extrapolation model, Moses et al. (2020) showed that the center of the region exhibiting the lowest $A_{\rm He}$ is situated between two closed-loop systems. Beyond the latitude range of $\pm$15° and beyond the distance of 1.7 R_s where magnetic field lines are mostly open, the relative helium abundance increases. They attributed these changes in helium abundance to the Coulomb drag, which depends on the velocity of solar wind, and gravitational settling in the closed field region. In open field line regions, lesser expansion factors cause higher speed, resulting in the higher $A_{\rm He}$. In Figure 2 we show for context the Carrington rotation obtained from NISP National Solar Observatory (NSO) Integrated Synoptic Program centered on the HERSCHEL observation date with the potential field source surface (PFSS) model where the open and closed field regions and the tilted-streamer-belt structure are evident, consistent with the modeling results discussed in Section 4 below. In Figure 2 of Moses et al. (2020), it is apparent that the helium intensity and abundance latitudinal dependence minima at heights 1.7, 1.9, and 2.1 R_s are a few degrees below the 270° latitude. The potential magnetic field extrapolation of the double streamer structure presented in Figure 3 of Moses et al. (2020) is not well consistent with the overall tilted-streamer-belt structure at solar minimum shown in Figure 2 and the closed magnetic field in the equatorial region. Since the gravitational settling of He^{++} is taking place in a closed field of a quiescent streamer and the Coulomb friction enhancement is taking place in an open field as demonstrated in past multifluid models, the single streamer-belt structure provides

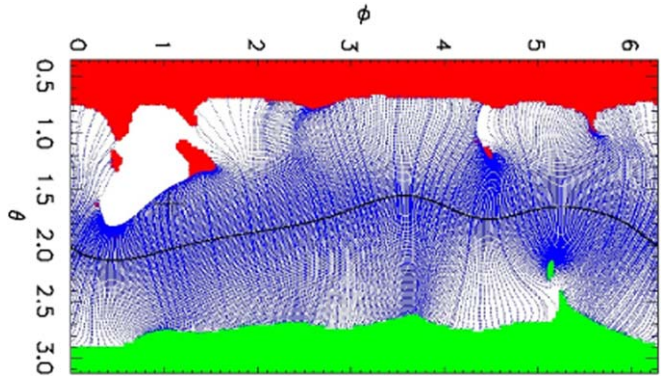

Figure 2. Representation of global magnetic field topology from PFSS model (Wang & Sheeley 1992) for the Carrington rotation centered on the HERSCHEL observation date (model available at NISP NSO Integrated Synoptic Program). The closed field lines are plotted in blue, and regions of open positive and negative flux are represented by green and red, respectively. The neutral line is drawn in black.

more consistent magnetic field structure with the observed helium emission.

In their Figure 2, Moses et al. (2020) show the latitudinal variation of the He abundance at the west solar limb derived from SCORE measurements at several heights and found that the He^{++} relative abundance decreases by an order of magnitude at the center of the streamer belt compared to the open field regions, i.e., in the closed field regions in which the plasma is mainly confined. The corresponding variation of H I in this region was found to be small with overall increase and some dips in intensity. Thus, it is likely that the difference in proton and He^{++} abundance variability arises from ion-dependent physical processes such as gravitational scale-height dependent ($H = k_B T_i/m_i g_s$, where k_B is Boltzmann's constant, T_i is ion temperature, m_i is the ion mass, and g_s is the solar gravitational acceleration) settling in the plasma confined to closed magnetic field regions. The observed depletion of helium abundance in the slow solar wind was studied recently using Wind data at 1 au and Parker Solar Probe data at perihelia in Yogesh et al. (2024), where they suggest that quiescent streamer cores are the preferred locations for gravitational settling to occur. This settling can cause a very low helium abundance, even below 1% in the solar wind protons. The role of these physical processes is demonstrated using the 3D three-fluid model in upcoming sections.

3. Description of the 3D Multifluid Model

In previous multifluid studies, the streamer model incorporated a heavy ion population as an additional fluid alongside plasma electrons and protons (see the review, Abbo et al. 2016). The plasma is characterized using a three-fluid approximation encompassing electrons, protons, and heavier ions, treated as coupled fluids influenced by collisional and electromagnetic interactions. This approximation extends well beyond the capabilities of single-fluid magnetohydrodynamics (MHD) description. The model assumes quasineutrality of the plasma and neglects electron inertia, employing $m_e \ll m_p$ to solve the electron momentum equation for the electric field (i.e., generalized Ohm's law). The electron density is derived from the charge neutrality condition. Notably, viscosity and explicit thermal conduction terms are disregarded in this model. The 2.5D three-fluid model was first developed for streamers with O^{5+} and He^{++} ions (e.g., Ofman 2000, 2004a; Li et al. 2006; Ofman et al. 2011). The 3D three-fluid model with O^{5+} ions of a slow solar wind in a tilted streamer belt was presented in Ofman et al. (2015), while here we include He^{++} ions as the third fluid. The normalized equations employed in the three-fluid model and the detailed description are given in Ofman et al. (2015). Below, we review the main model parameters relevant to the present study.

In the model equations shown in Ofman et al. (2015), the index $k = e, p, i$ represents electrons, protons, or heavier ions (in the present study He^{++}), where n_k denotes the number density, V_k is the velocity vector, T_k is the temperature for each species, S_k is the empirical heating term (only used for He^{++} ions), $S_{r,e}$ is the electron radiative loss term, $\delta_{k,e}$ is the Kronecker delta, C_{kjl} is the energy coupling term between the species (Ofman 2004a), and γ_k is the polytropic index of each species. Empirical polytropic indices of $\gamma_k = 1.05$ are assumed to model the effects of coronal heating and heat conduction losses for electrons, protons, and He^{++} ions consistent with the approach in some global coronal models, e.g., Riley et al. (2006). These empirical values of $\gamma_k > 1$ allow realistic multifluid modeling of the coronal streamer constituent temperatures in agreement with observations (e.g., Ofman et al. 2011). The terms proportional to ion gyrofrequency are neglected in the low-frequency limit, and the time is normalized in units of the Alfvén time $\tau_A = R_s/V_A$, where the Alfvén speed is $V_A = B_0/\sqrt{4\pi m_p n_{e0}}$ defined here with the proton mass, B_0 is the normalization magnetic field strength (in the present study we set $B_0 = 7$ G), m_p is the proton mass, and n_{e0} is the normalization value of the electron number density. Using $n_{e0} = 5 \times 10^8\ \mathrm{cm}^{-3}$, we get $V_A = 683\ \mathrm{km\ s}^{-1}$. For He^{++} we have $A_{He^{++}} = 4$ and $Z_{He^{++}} = 2$. The other model parameters are S the Lundquist number (here, we set $S = 10^4$, a typical numerical resolution-limited value in MHD models that does not significantly affect the result); electron and proton Euler number $\mathrm{Eu_{e,p}} = (k_b T_{0,e,p}/m_p) V_A^{-2}$; ion Euler number $\mathrm{Eu_i} = (k_b T_{0,i}/m_i) V_A^{-2}$; and Froude number $F_r = V_A^2 R_S/GM_S$, where G is the universal gravitational constant and M_S is the solar mass, R_S is the solar radius, $b = cB_0/(4\pi e n_{e0} R_S V_A)$ is the normalization constant, k_b is the Boltzmann constant, and $F_{k,\mathrm{coul}}$ is the Coulomb friction (or drag) terms proportional to the velocity differences between the species and the collision frequencies (see, e.g., Braginskii 1965; Geiss et al. 1970; Ofman & Davila 2001, for details of these terms). The empirical heating term for He^{++} ions is the function $S_i = S_{i0}(r-1)\ e^{-(r-1)/\lambda_{i0}}$, where the constants S_{i0} and λ_{i0} determine the magnitude and the decrease of the heating rate with distance r. In the present model, we use the empirical values $S_{i0} = 7.25$ and $\lambda_{i0} = 0.5\ R_s$ constrained by radial density and temperature structure of He in open field regions (e.g., Ofman 2004b). The initial temperatures were uniform ($T_e = T_p = 1.6$ MK, $T_{He} = 4$ MK) and evolve self-consistently. For simplicity, the possible effects of ion temperature anisotropy are neglected in this model.

These equations are evolved numerically in a 3D spherical domain using the fourth-order integration method until a quasi-steady streamer belt is formed (see Ofman et al. 2015, for details). The ranges for spatial coordinates are $1\ R_s \leqslant r \leqslant 7\ R_s$, $0 < \theta < \pi$ and $0 < \phi < 2\pi$, with a small circular region around the poles removed to avoid singularity of the coordinate system. The computation started with a tilted-dipole (with a tilt of 10° with respect to the solar rotation axis) coronal magnetic

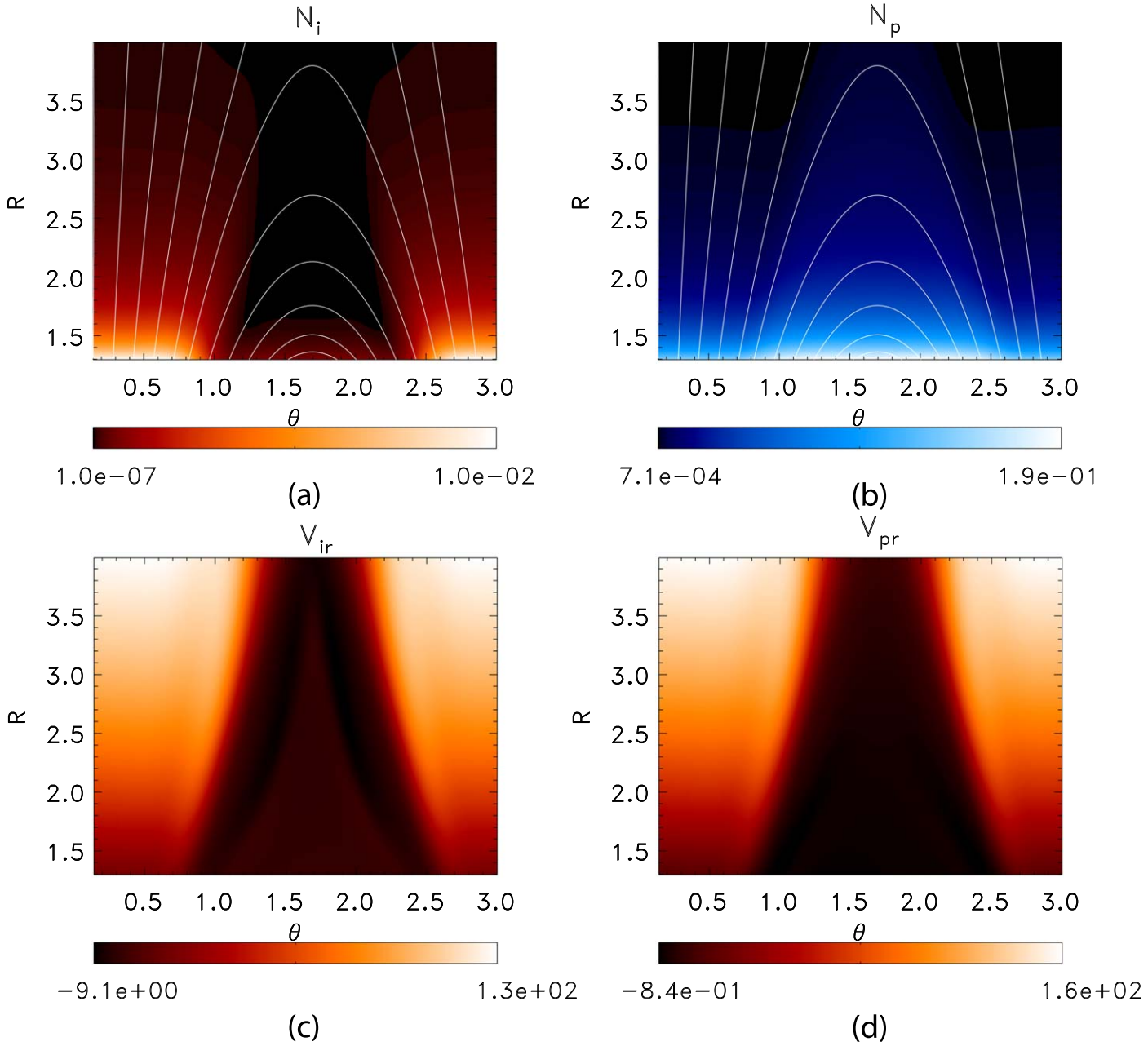

Figure 3. The results of the 3D three-fluid model of the tilted streamer belt shown in the r–θ plane at longitude $\phi = 0.76$ rad. The distance is in solar radii, and angles are in radians. The densities are normalized in terms of $n_{e0} = 5 \times 10^8$ cm^{-3}. The white lines mark several field lines of the modeled magnetic field. (a) The normalized density of the He^{++} ions. (b) The normalized proton density (blue). (c) The He^{++} radial velocity in km s^{-1}. (d) The proton radial velocity in kilometers per second.

field model (Ofman et al. 2015). The following boundary conditions are implemented in the simulation. At the inner boundary $r = 1$ R_s, the magnetic field components are fixed (line tied), and the values of density, temperature, and velocity components at the boundary grid cells are extrapolated from the first interior cells with zero gradients, approximating outgoing characteristics (Steinolfson & Nakagawa 1976). At the outer boundary $r = 7$ R_s, open boundary conditions are set for all variables. The outer boundary distance is chosen to satisfy supersonic slow solar wind transition. The presented results were obtained with a uniform resolution of $160 \times 128 \times 508$ grid cells in the θ, ϕ, and r domains, respectively. The results were also tested for convergence with a higher-resolution (albeit shorter duration) run, and no significant changes were observed with higher-resolution solutions.

4. Numerical Results

Here, we present the results of our 3D three-fluid model of streamer belt with He^{++} for the titled dipole initial state and the parameters given in Section 3. The solutions are obtained by running the model to quasisteady state, where the initial tilted-dipole field evolves to a streamer-belt solution (as in Ofman et al. 2015 but with O^{5+}). In Figure 3 we show the section of the streamer belt in the r–θ plane cut at $\phi = 0.76$ rad in the radial extent $1.3\ R_s \leqslant r \leqslant 4\ R_s$, similar to the radial extent covered by HERSCHEL observations. The white lines mark several closed and open field lines in this plane. It is evident that the slow solar wind outflow velocity v_r is significant outside the streamer core, and velocities are small inside the streamer core for both protons and He^{++}. The corresponding

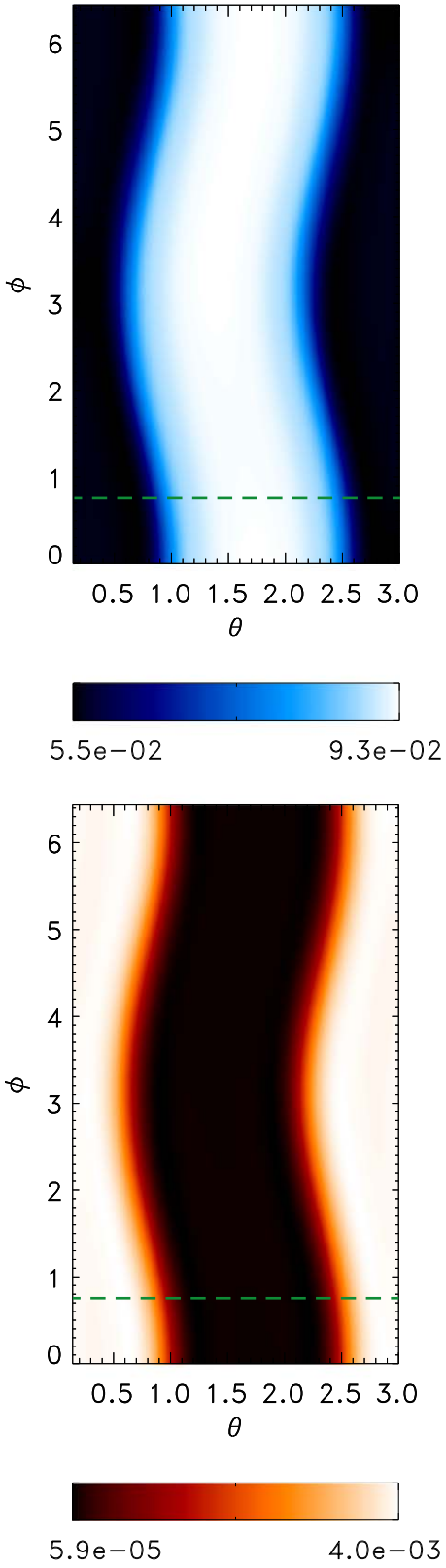

Figure 4. The results of the 3D three-fluid model of the tilted streamer belt shown in the $\theta-\phi$ [rad] plane at the height of $r = 1.5\ R_s$. The densities are normalized in terms of $n_{e0} = 5 \times 10^8\ \mathrm{cm}^{-3}$. Left panel: the normalized proton density. Right panel: the normalized density of the He^{++} ions. The dashed green line marks the longitude of the $\theta-r$ plane cuts in Figure 3.

density structure of the He^{++} dips significantly at the closed field core of the streamer and peaks in the open field streamer flanks. The proton density structure shows the opposite latitudinal dependence and peaks in the streamer core. This streamer density structure is in good qualitative agreement with observation in the region where A_{He} was determined, shown in Figure 1.

In Figure 4 we show the density structure of the tilted streamer belt in the $\phi-\theta$ plane (i.e., analogous to a Carrington map but for density) at the height of $r = 1.5\ R_s$. The apparent sinusoidal structure of the streamer belt is due to the 10° tilt projected onto the plane, and the higher proton density in the streamer core, anticorrelated with the He^{++} density, is evident in the tilted-streamer-belt structure. The modeled tilted-streamer-belt structure is consistent with the Carrington map of the streamer belt for the solar minimum conditions during HERSCHEL observations shown in Figure 2.

Figure 5 is devoted to the latitudinal dependence of the variables across the streamer belt shown at a height of 1.75 R_s. The radial velocities v_r of protons (solid line) and He^{++} (dashes) are shown in Figure 5(a). The outflow velocities of the two ions are close due to the effects of the Coulomb friction terms with magnitude that is proportional to the velocity difference of the electrons, protons, and He^{++} ions (the F_k terms in the momentum equation). The effect of the Coulomb friction is to reduce the differential flow of the three fluids. The modeled solar wind velocity outside the streamer is consistent with observational values (Abbo et al. 2010; Ofman et al. 2011). It is evident that inside the streamer belt, the velocities are very low so that the plasma can be considered nearly static. The small downflow velocity of He^{++} is associated with gravitational settling. The anticorrelated normalized density structures of protons and He^{++} ions are shown in Figure 5(b). The densities are normalized with the corresponding densities at $\theta = 3$ rad. The temperatures of protons, He^{++} ions, and electrons obtained from the three-fluid model are shown in Figure 5(c). It is evident that the He^{++} ions remain hotter than the other fluids due to the overall effect of the ion heating term. However, in the core of the quiescent streamer, the He^{++} temperature is larger than in the open field region due to the thermal energy exchange and cooling by the protons and electrons. It is also evident that in the core the quiescent streamer, the electron and proton temperatures are nearly identical due to the thermal energy exchange terms that tend to minimize the temperature difference between the species when collisions are significant.

5. Discussion and Conclusions

The variability of helium abundance in the solar wind and the solar corona is a puzzling phenomenon that provides clues on the SC, type of the solar wind (fast or slow), and possibly on the acceleration processes and on the origins of the solar wind (e.g., Alterman & Kasper 2019). However, the processes that lead to the variability of helium in the corona are not well understood so far. The observation of UV helium emission is not routinely available in coronal streamers. The only available observations so far are the provided UV imaging of streamers in both H I and He II emission using the HERSHEL rocket experiment reported recently by Moses et al. (2020). It is

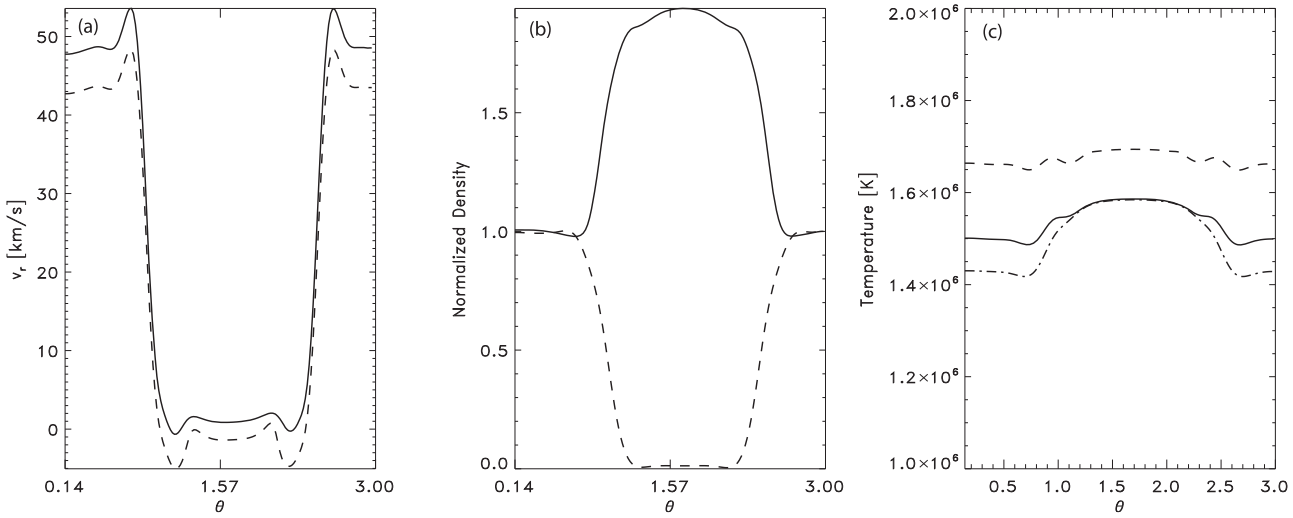

Figure 5. The cross-sectional cut of the variables at $r = 1.75\ R_s$ for the model run shown in Figure 3 (solid: protons; dashes: He^{++} ions; dotted–dashed: electrons). (a) The outflow velocities V_r. (b) The densities normalized by the values at maximal θ. (c) Proton, He^{++}, and electron temperatures.

evident from the imaging data of the inner corona that the emission of hydrogen and helium is overall anticorrelated, suggesting that different processes shape the helium abundance in streamers than hydrogen, as predicted by past three-fluid models. Moreover, the potential magnetic field extrapolation model double streamer magnetic structures shown in Moses et al. (2020) does not account well for the gravitational settling of He^{++} in a quiescent streamer core at the equatorial region nor with the overall magnetic structure of an equatorial streamer belt at solar minimum.

We use the 3D three-fluid model with electron, proton, and He^{++} ion fluids to compute the tilted-streamer-belt structure in the inner corona in the region observed by HERSHEL instruments. We find good qualitative agreement of the observed streamer structure of protons and He^{++} ions that also agrees with previous, more simplified 2.5D three-fluid models of the slow solar wind in coronal streamers, as well as the 3D model with O^{5+} ion as the third fluid with depleted equatorial streamer-belt core helium abundance and enhanced helium abundance in the open field regions. Specifically, Moses et al. (2020) computed the helium relative abundance shown in their Figure 3 from the ratio of the H I and He II emissions, and we find that these results are in qualitative agreement with our three-fluid modeling results.

The present model shows that the main processes that shape the distinct helium streamer structure and slow solar wind helium abundance are gravitational settling of He^{++} in the core of the quiescent streamer closed field region as well as collisional and thermal coupling of He^{++} ions to the electrons and protons in the magnetiaed plasma. The increased He^{++} relative abundance in the open field region is produced by the velocity-dependent Coulomb friction process with the outflowing electrons and protons, which tend to minimize differences between the fluids and as a result "drags out" the heavier He^{++} ions. It is interesting to note that the observed depleted He^{++} and the enhanced protons abundance in the streamer-belt core are captured by the idealized tilted-streamer-belt structure appropriate for solar minimum conditions and do not require a complex multiple-streamer configuration suggested in the past (Noci et al. 1997; Moses et al. 2020). However, reproducing finer details of the observation would indeed require more realistic magnetic field structure in the 3D multifluid model, as well as detailed emission calculations and line-of-sight integration, and these are left for future studies. Our modeling results that find very low helium abundance in the core of the streamer are in agreement with recent in situ observations of low A_{He} at 1 au traced back to coronal streamer structures (Yogesh et al. 2024). The present results extend the previous three-fluid modeling studies with He^{++} to a more realistic 3D tilted-streamer-belt structure, appropriate for solar minimum conditions.

Acknowledgments

We would like to acknowledge discussions with Dr. Lucia Abbo. L.O. and Y. acknowledge support by NSF grant AGS-2300961, L.O. acknowledges support by NASA LWS grant 80NSSC20K0648. Resources supporting this work were provided by the NASA High-End Computing (HEC) Program through the NASA Advanced Supercomputing (NAS) Division at Ames Research Center. We would like to acknowledge high-performance computing support from Cheyenne (doi:10.5065/D6RX99HX) provided by NCAR's Computational and Information Systems Laboratory, sponsored by the National Science Foundation.

ORCID iDs

Leon Ofman https://orcid.org/0000-0003-0602-6693
Yogesh https://orcid.org/0000-0001-6018-9018
Silvio Giordano https://orcid.org/0000-0002-3468-8566

References

Abbo, L., Antonucci, E., Mikić, Z., et al. 2010, AdSpR, 46, 1400
Abbo, L., Ofman, L., Antiochos, S. K., et al. 2016, SSRv, 201, 55
Alterman, B. L., & Kasper, J. C. 2019, ApJL, 879, L6
Asplund, M., Grevesse, N., Sauval, A. J., & Scott, P. 2009, ARA&A, 47, 481
Borrini, G., Gosling, J. T., Bame, S. J., & Feldman, W. C. 1982, JGR, 87, 7370
Braginskii, S. I. 1965, RvPP, 1, 205
Fineschi, S., Antonucci, E., Romoli, M., et al. 2003, Proc. SPIE, 4853, 162
Geiss, J., Hirt, P., & Leutwyler, H. 1970, SoPh, 12, 458
Giordano, S., Fineschi, S., Ofman, L., Mancuso, S., & Abbo, L. 2007, in ESA Special Publication, Second Solar Orbiter Workshop, 641, ed. E. Marsch et al. (Paris: ESA), 31
Grevesse, N., & Sauval, A. J. 1998, SSRv, 85, 161
Kasper, J. C., Stevens, M. L., Korreck, K. E., et al. 2012, ApJ, 745, 162

Kasper, J. C., Stevens, M. L., Lazarus, A. J., Steinberg, J. T., & Ogilvie, K. W. 2007, ApJ, 660, 901
Laming, J. M., & Feldman, U. 2001, ApJ, 546, 552
Laming, J. M., & Feldman, U. 2003, ApJ, 591, 1257
Li, B., Li, X., & Labrosse, N. 2006, JGR, 111, A08106
Moses, J. D., Antonucci, E., Newmark, J., et al. 2020, NatAs, 4, 1134
Neugebauer, M., Goldstein, B. E., Smith, E. J., & Feldman, W. C. 1996, JGR, 101, 17047
Noci, G., Kohl, J. L., Antonucci, E., et al. 1997, in ESA Special Publication, Fifth SOHO Workshop: The Corona and Solar Wind Near Minimum Activity, 404, ed. A. Wilson (Paris: ESA), 75
Ofman, L. 2000, GeoRL, 27, 2885
Ofman, L. 2004a, AdSpR, 33, 681
Ofman, L. 2004b, JGR, 109, A07102
Ofman, L., Abbo, L., & Giordano, S. 2011, ApJ, 734, 30
Ofman, L., & Davila, J. M. 2001, ApJ, 553, 935
Ofman, L., & Kramar, M. 2010, in ASP Conf. Ser. 428, SOHO-23: Understanding a Peculiar Solar Minimum, ed. S. R. Cranmer, J. T. Hoeksema, & J. L. Kohl (San Francisco, CA: ASP), 321
Ofman, L., Provornikova, E., Abbo, L., & Giordano, S. 2015, AnGeo, 33, 47
Riley, P., Linker, J. A., Mikić, Z., et al. 2006, ApJ, 653, 1510
Steinolfson, R. S., & Nakagawa, Y. 1976, ApJ, 207, 300
Wang, Y. M., & Sheeley, N. R., Jr. 1992, ApJ, 392, 310
Yogesh, Chakrabarty, D., & Srivastava, N. 2021, MNRAS, 503, L17
Yogesh, Chakrabarty, D., & Srivastava, N. 2022, MNRAS, 513, L106
Yogesh, Chakrabarty, D., & Srivastava, N. 2023, MNRAS, 526, L13
Yogesh, Gopalswamy, N., Chakrabarty, D., et al. 2024, ApJ, submitted